

EXAMINATION OF SUSCEPTIBILITY EFFECTS ON FUNCTIONAL AND DYNAMIC
MAGNETIC RESONANCE IMAGING

BY

THOMAS LE PAINE

THESIS

Submitted in partial fulfillment of the requirements
for the degree of Master of Science in Bioengineering
in the Graduate College of the
University of Illinois at Urbana-Champaign, 2011

Urbana, IL

Adviser:

Assistant Professor Brad Sutton

ABSTRACT

A homogeneous, static magnetic field is important in magnetic resonance imaging. When a homogeneous field is not present it can cause imaging artifacts and misestimation of tissue structures, flow, and brain function. However, magnetic field inhomogeneity also drives certain contrast mechanisms including blood oxygenation level dependent fMRI. The two projects in this work look at the effects of inhomogeneity on functional and dynamic MRI. We simultaneously acquired functional and dynamic MRI (Simulscan) of natural un-cued swallows. Work was done to minimize susceptibility artifacts in the dynamic images, but still have susceptibility induced BOLD contrast in functional MRI, but some residual susceptibility issues remained.

We analyzed these residual susceptibility issues in BOLD, and develop a calibration procedure to remove these effects. This work focuses in-plane gradients of the magnetic field that result in spatially-varying BOLD sensitivity. These artifacts depend on subject-specific magnetic-field distributions in the brain as well as acquisition. To correct these spatially-varying BOLD-sensitivity artifacts, a calibration for percent-signal-change measures is developed.

ACKNOWLEDGMENTS

I must express my earnest thanks to everyone that helped make this research project possible. My sincerest thanks goes to my adviser, Professor Brad Sutton, for his help in preparing this manuscript. And a special thanks goes to my friends and family who have helped me when things have gotten tough.

TABLE OF CONTENTS

1. Introduction.....	1
1.1. Basic MR Physics.....	2
1.2. Image Reconstruction.....	4
1.3. Magnetic-Field Inhomogeneity.....	5
1.4. Functional MRI.....	6
2. Balancing Image Distortion and Functional Contrast from Susceptibility: Simultaneous Dynamic and Functional MRI Scanning (SimulScan) of Natural Swallows	9
2.1. Introduction	9
2.2. Methods	12
2.3. Results	16
2.4. Discussion and Conclusion	20
3. Calibration to Remove Spatial Variation in BOLD Response from Susceptibility Gradient.....	24
3.1. Introduction	24
3.2. Theory	26
3.3. Methods	29
3.4. Results	33
3.5. Discussion	40
3.6. Conclusion.....	42
References.....	43

1. INTRODUCTION

Magnetic resonance imaging (MRI) relies on a large, homogeneous, static, magnetic field to localize protons and provide information about water content, tissue structures, metabolic contents, flow, and brain function. Disruptions to the homogeneity of the magnetic field can serve useful purposes, such as providing information about brain function through iron in hemoglobin, a process called the blood oxygenation level dependent (BOLD) response. Or it can disrupt the image formation process by causing spatial variations in proton frequencies. The purpose of this thesis is to describe the challenges and use of magnetic susceptibility effects in studying cognitive and motor brain functions. The first project applies a simultaneous dynamic and functional imaging acquisition to swallowing. Our developed method minimizes susceptibility impacts on dynamic imaging while maintaining sensitivity to functional neuroimaging signals from hemoglobin-related susceptibility changes. This method has many benefits over existing swallowing functional acquisitions, which must use separate monitoring devices that may alter the motion of swallowing and related brain activity. Also it opens up new methods for studying swallowing motion and brain function in concert. The second project looks at BOLD sensitivity artifacts caused by in-plane gradients in the magnetic field due to susceptibility differences near air/tissue interfaces. Previous work has been done in the field, including in-acquisition correction techniques. We analyze the effects for different acquisition trajectories and develop and validate a post-processing calibration technique to remove the susceptibility-gradient-induced spatial variability of BOLD sensitivity.

Each project is described in its own chapter. While these projects are related through their treatment of magnetic-susceptibility effects, each has a unique set of background literature, which will be presented in the introduction section of each chapter. Here we will present an overview of topics relevant to both projects,

including basic MR physics, image reconstruction, magnetic-field inhomogeneity, and functional MRI.

1.1. Basic MR Physics

In magnetic resonance imaging, many elements – including a large main magnetic field, resonance phenomena, and imaging gradients – must work together to produce an image. The large magnetic field, B_0 , is used to prepare the nuclei of the object to be imaged. The magnetic field must fulfill two properties: it must be strong to polarize the spins of the nuclei, giving rise to a bulk magnetic moment; and must be uniform across the object so that its nuclei are all treated equally (We will discuss what happens when the field is not uniform later). The strong magnetic field causes the spins to polarize. With spin $\frac{1}{2}$ particles such as protons, the spins can be in two possible energy states, low and high. At room temperature slightly more spins are in the high-energy state compared to the low-energy state. The result is a net magnetic moment that is pointing in the direction of B_0 . This bulk magnetic moment can then be manipulated as described below.

The magnetic field must be uniform so that all the nuclei across the object will precess at the same frequency, the Larmor frequency, given by:

$$\omega_0 = \gamma B_0, \tag{1}$$

Where γ is the gyromagnetic ratio, a physical constant that depends on the type of nuclei. It tells how fast a particular nucleus will precess when a certain magnetic field is applied. For proton the gyromagnetic ratio is 42.58 MHz/T. When an object is first put into the scanner, all MR-active nuclei are precessing. It is not until the imaging experiment begins that a specific nuclei is chosen by resonance frequency pulses.

The goal of the imaging experiment is to prepare the contrast of the image, and to sample enough data that the object can be reconstructed. An imaging experiment has two main stages, excitation and readout. In the excitation stage, magnetic fields oscillating at the same frequency as the Larmor frequency of the nuclei of interest are briefly turned on. These are called RF pulses. The RF pulses tip

the bulk magnetization vector out of alignment with the main magnetic field, towards the transverse plane. When the RF pulse is turned off, the magnetization vectors continue to precess at the Larmor frequency. The magnetization oscillating in the transverse plane may now be detected by the coils in the MR scanner, by Faradays law of induction. The coils see a superposition of all the spins oscillating together. This phenomenon is the basis for NMR. To create an image, requires the readout stage of the imaging experiment. Other RF frequency pulses, and magnetic-field gradients can be turned on during the excitation stage to give specific contrasts. In this work, we will focus on gradient-echo (GRE) acquisitions in which the image $i(r)$ is weighted primarily by the proton density $\rho(r)$, and $T2^*$.

The next stage of the imaging experiment is readout. Here, magnetic fields are applied whose amplitude vary linearly across the object. These are the magnetic field gradients, G_x , G_y , G_z . These alter the precession of the spins

$$\omega(x, y, z) = \gamma(B_0 + G_x x + G_y y + G_z z), \quad (2)$$

By applying them, and demodulating the measured signal by the resonance frequency ω_0 we are able to sample the spatial Fourier domain of the object,

$$s(\vec{k}) = \int_R i(\vec{r}) e^{-j\vec{k} \cdot \vec{r}} d\vec{r}, \quad (3)$$

Where the spatial domain variable is the gradients integrated over time

$$k_x = \gamma \int_0^t G_x t' dt' \quad (4)$$

When sampling k-space, the most intuitive approach is to sample a line of k-space, followed by another line, followed by another. This is called Cartesian sampling (Figure 1b). Non-Cartesian sampling trajectories, such as spiral (Figure 1a) (1) and radial projection, are used for various reasons, such as faster imaging time due to more efficient coverage of k-space.

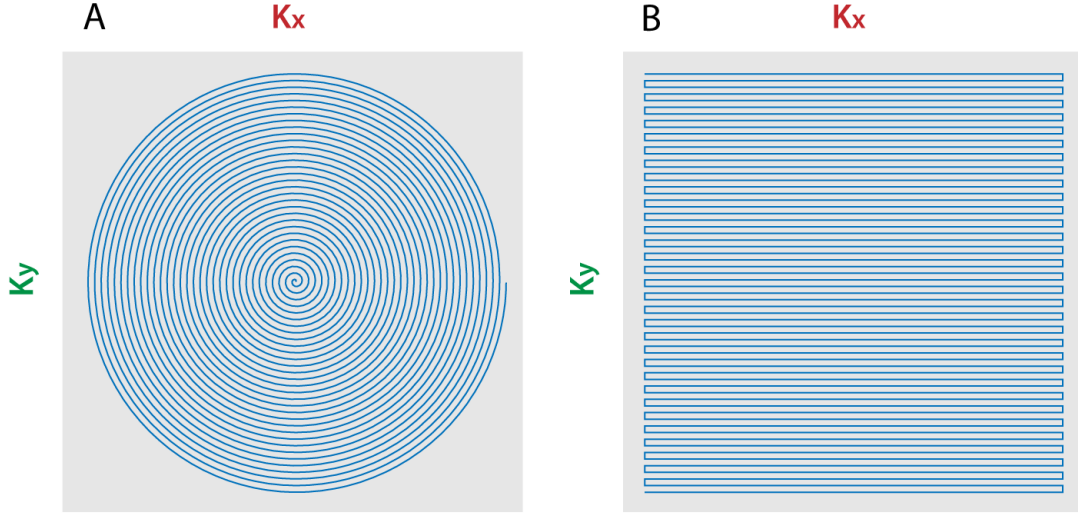


Figure 1. Diagrams of two common k-space sampling trajectories (a) spiral and (b) Cartesian.

1.2. Image Reconstruction

To obtain the image from the data measured, a model of the imaging experiment is used. The most basic model is a basic Fourier transform

$$i(\vec{r}) = \int_K s(\vec{k}) e^{j\vec{k} \cdot \vec{r}} d\vec{k} \quad (5)$$

However, we only have discrete samples of the object, so the problem is ill-posed.

We can discretize the problem by converting from continuous to discrete through the use of a basis expansion. For Cartesian sampling the differential area, dk from the integral equation, is uniform and we can rewrite this in discrete Fourier

Transform form as

$$i_n = \sum_{m=0}^{M-1} s_m e^{jk_m r_n}, n = \{0, 1, \dots, N-1\} \quad (6)$$

And because of the uniformly sampled nature of the r and k sequences, this can be performed using the fast Fourier transform (FFT), making the reconstruction significantly faster.

When non-Cartesian trajectories are used, we see that the area surrounding each k-space sample is non-uniform. This translates into a weighting term w , often called the sample density compensation factor, which represents the Jacobian of a transformation from non-uniformly spaced k-space samples to uniformly spaced time samples (2, 3). For certain sampling trajectories, this factor can be calculated using just the derivative of the k-space trajectory. In other cases such as multi-shot imaging different methods have been used including Voronoi areas. Not taking this factor into account can have a very strong effect on the resulting image.

$$i_n = \sum_{m=0}^{M-1} w_m s_m e^{jk_m r_n}, n = \{0, 1, \dots, N-1\} \quad (7)$$

Another downside of non-Cartesian reconstruction is that because we are not sampling on a Cartesian grid, the FFT cannot be applied directly. Instead we use the Discrete Fourier Transform. This is sometimes also called the conjugate phase reconstruction method. This results in relatively long computation times. These times can be decreased by interpolating the data on to a Cartesian grid, and then using the FFT, a process called gridding (4, 5).

1.3. Magnetic-Field Inhomogeneity

The above development assumed that the main, static, magnetic field was homogeneous. This is often not the case for two reasons. First, hardware limitations make high-strength, homogeneous, magnetic fields difficult to achieve, so shimming coils must be added to compensate for lower-order inhomogeneity terms. These problems are more pronounced at 3T compared to 1.5 T, and again are more pronounced at 7T (6). Second, materials placed in a magnetic field respond by generating additional magnetic field, as determined by the material magnetic susceptibility. If the magnetic susceptibility between two materials located near each other is different, it causes large field inhomogeneities. Often, this variation in the spatial distribution of the magnetic field is represented by $\Delta B(r)$, referred to as

the field map. The frequency of precession of protons subjected to this deviation in magnetic field has been altered

$$\omega(\vec{r}) = \gamma(B_0 + \Delta B(\vec{r})), \quad (8)$$

And the frequency deviation caused by inhomogeneity is given by

$$\Delta\omega(\vec{r}) = \gamma\Delta B(\vec{r}), \quad (9)$$

This term enters into the signal model giving

$$s(\vec{k}) = \int_R i(\vec{r}) e^{-j\gamma\Delta\omega(\vec{r})t} e^{-j\vec{k}\cdot\vec{r}} d\vec{r}, \quad (10)$$

While the signal encoding is still linear, it is now shift variant. Each voxel has a unique phase evolution caused by the magnetic-field inhomogeneity. The zeroth-order effects of inhomogeneity cause spatially-varying point spread functions. For Cartesian sampling this appears as geometric shifts, and in non-Cartesian sampling it appears as blurring. In addition, the first-order effects of the inhomogeneity cause local k-space trajectory distortions, which will be discussed further in Chapter 3.

1.4. Functional MRI

Functional MRI (fMRI) is the most used method of analyzing brain activation. The primary goal in MRI is to localize neuronal activity. However, it is not possible to detect this directly, instead neuron-related blood-oxygenation-level-dependent (BOLD) signals are detected. This provides fMRI with a spatial resolution limited by the microvasculature, and temporal resolution limited by speed of the hemodynamic response. Typical spatial resolutions are approximately 1-3 mm³ and the time delay of the hemodynamic response is a few seconds.

Detecting the blood-oxygenation-level-dependent (BOLD) signal is done by detecting magnetic-susceptibility changes that depend on the oxygenation state of hemoglobin. Deoxyhemoglobin has a magnetic susceptibility that is very different than surrounding tissues. Magnetic-susceptibility differences result in microscopic magnetic-field inhomogeneity which dephase proton spins within a voxel and cause signal loss. During functional activation a specific time-course of activity occurs

called the hemodynamic response. The most notable feature in the hemodynamic response is increased flow of oxyhemoglobin causing deoxyhemoglobin concentration to decrease, magnetic-field homogeneity to increase, and the measured signal to increase.

In order to maximize the BOLD contrast from deoxygenated vs. oxygenated blood, an imaging experiment must be sensitive to differences in magnetic susceptibility. Recall that, gradient-echo (GRE) acquisitions are T2* weighted, which makes them sensitive to magnetic field non-uniformities, and in turn susceptibility differences. GRE acquisitions also amplify macroscopic magnetic-susceptibility differences that exist near air/tissue interfaces at locations such as orbitofrontal cortex and medial temporal lobes. Since air and tissue differ in magnetic susceptibility, variations in the magnetic field are created in brain regions where air/tissue interfaces occur.

Typically in an fMRI experiment, a time-series of GRE images is acquired while a functional task is presented. The task can be a block design, where a task is performed for an extended duration followed by a rest state, and the active and rest blocks are repeated many times (Figure 2).

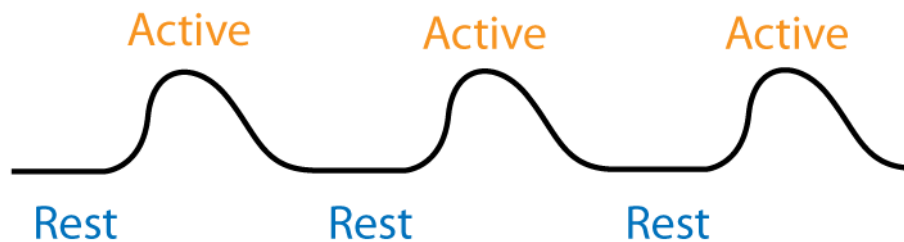


Figure 2. Illustration of expected voxel time-series for a simple block design task.

Event related designs are also used, where a brief task event is performed at random intervals through the experiment (7,8). This allows many task types to be presented during the course of the experiment, and can be optimized for best event separation.

The end result in fMRI is usually a statistical map showing areas that correlate with the expected activation given the presented task. The statistical analysis is performed for each voxel time-series by general linear modeling, wherein a model regressor for each task is created by convolving the task stimulus times with the expected hemodynamic response. Another model regressor accounts for the mean of the data. The model is then applied to the measured fMRI time-series and each regressor receives a beta weight. These are used, along with the residual variance in the time series, to generate the statistical map, and to calculate another commonly used metric, percent signal change (PSC). Here PSC is approximated as

$$PSC(\vec{r}) = \frac{\beta_{task}(\vec{r})}{\beta_{mean}(\vec{r})}, \quad (11)$$

2. BALANCING IMAGE DISTORTION AND FUNCTIONAL CONTRAST FROM SUSCEPTIBILITY: SIMULTANEOUS DYNAMIC AND FUNCTIONAL MRI SCANNING (SIMULSCAN) OF NATURAL SWALLOWS¹

2.1. Introduction

As we saw in Chapter 1, magnetic-susceptibility differences can be used to examine brain function through the BOLD effect. However, macroscopic magnetic field inhomogeneity resulting from air/tissue interfaces can disrupt accurate imaging. In this chapter, we examine the study of the neuromuscular control of swallowing, an area where the good and the bad of magnetic susceptibility meet, creating a challenging imaging environment. We demonstrate our balance of susceptibility-induced distortions, maintenance of BOLD contrast, and balance of acquisition speed for functional and dynamic imaging.

Swallowing is a complicated coordination of central and peripheral sensorimotor behaviors that is necessary for sustaining life. Nearly 40 pairs of bilaterally innervated muscles must be activated in proper sequence for a completely functional swallow. This coordinated process transforms the aerodigestive tract from a path for air movement, to a duct for food and fluids (9). The transformation seals the tract, preventing nutritive materials from entering and clogging the airway during its transportation to the pharynx. Fundamental to proper swallowing is involvement of cortical, subcortical and brainstem areas. Dysphagia, i.e., difficulty swallowing, may result from failure in the central neural and peripheral sensorimotor systems, and may lead to malnutrition, dehydration and respiratory problems (9). Risk for dysphagia increases with age, and it can be caused by numerous neurogenic diseases such as stroke, dementia, Alzheimer's Disease, Parkinson's Disease, cerebral palsy, and traumatic brain injury (10).

¹ This work is based on a previous publication: Paine, T. L., Conway, C. A., Malandraki, G. A., & Sutton, B. P. (2011). Simultaneous dynamic and functional MRI scanning (SimulScan) of natural swallows. *Magnetic Resonance in Medicine*, 65(5), 1247–1252. The copyright owner has provided permission to reprint.

MRI has proven to be a useful tool for studying both the central and peripheral sensorimotor levels of swallowing using both functional MRI and dynamic imaging. MRI research of swallowing and dysphagia has increased dramatically over the last decade and continues to provide promising results in understanding the mechanisms of age- and pathology-related changes. Cortical control of swallowing has been evaluated with functional MRI (10-14), and oropharyngeal muscle behaviors have been studied by dynamic MR imaging (15-22). However, few MRI studies have looked at integration of the neural control and oropharyngeal sensorimotor function, though such integrated studies may hold the key to studying more nuanced swallowing changes such as aged swallowing, i.e., presbyphagia (9), and difficulty planning deglutition, i.e., swallowing apraxia (23). Understanding the interaction between the central and peripheral sensorimotor behaviors could provide breakthrough clinical knowledge for patients with neurogenic dysphagia. To correctly identify and treat neurogenic swallowing disorders, a clear link must be made between neural activation and the corresponding sensory responses and muscle activations (10).

Dynamic MRI of swallowing visualizes soft tissues better than X-ray video fluoroscopy, where dense bone may obscure underlying soft-tissue movement. Additionally, X-ray fluoroscopy also requires use of ionizing radiation and a contrast agent (barium) must be swallowed for accurate judgments of the biomechanics of the swallow (24). A current significant advantage of X-ray fluoroscopy over MRI is its imaging speed, obtaining rates of 30 frames per second (fps) or faster. In contrast, MRI dynamic imaging has only recently achieved serial imaging rates of 20 fps with an optimized acquisition sequence (21-22). Imaging speeds at this rate or faster are required to temporally resolve many of the complex motions during swallows. For instance, velar elevation during swallowing is achieved in approximately 50 ms and velopharyngeal contact during the pharyngeal stage of swallows has been reported to take between 300 to 400 ms (25).

Besides imaging speed, another challenge for fast imaging with MRI in this region includes magnetic susceptibility differences that exist at air-tissue interfaces, which are abundant in the oropharyngeal region. The susceptibility differences

result in artifacts that depend on the sequence design. Susceptibility artifacts can be addressed in the acquisition, by splitting an acquisition into multiple shots, or during image reconstruction by using a susceptibility corrective reconstruction algorithm.

As previously stated, functional MRI non-invasively monitors brain activations associated with a performed task by examining local changes in blood oxygenation (26). Often the task is cued by visual or audio stimulus, instructing the subject when and what task to perform. The subject must perform the task in strict compliance with the stimulus for accurate fMRI statistical analysis. In fMRI studies investigating swallowing, secondary-monitoring devices including surface electrodes placed over the thyroid cartilage (14) or pneumographic belts placed around the neck (10-11), ensure the subjects' swallows comply with the stimuli. Such devices may result in sensory feedback, interfering with normal muscle function, motor planning and even brain activations. Alternatively, swallowing compliance may not be monitored. This is problematic as missed or delayed swallows may alter fMRI statistical results. Dynamic MRI images of the oropharyngeal region acquired simultaneous with fMRI would eliminate the need for extra equipment, and provide a consistent methodology for monitoring and reporting swallowing compliance. Also, it would allow covert monitoring of natural swallows.

In the present investigation an interleaved fMRI/dynamic MRI sequence (SimulScan) with joint acquisition of the cortical, subcortical and oropharyngeal systems was developed. This results in effectively simultaneous acquisition of fMRI/dynamic MRI data, as the repetition time is similar to existing approaches, and functional images are captured at a rate adequate for resolving the functional (BOLD fMRI) signal. The sequence was previously described in (27). The sequence eliminates the need for extra monitoring equipment, and provides a consistent methodology for monitoring and reporting swallowing compliance. SimulScan builds upon fast FLASH spiral sequences to provide interleaved acquisition, while maintaining dynamic imaging rates of 14.5 fps. The sequence utilizes a spiral k-space trajectory for which susceptibility changes result in blurring. Breaking the

spiral-design into multiple shots can minimize this blurring artifact to levels that do not interfere with interpretation of the motion (21).

The SimulScan sequence is applied to covertly monitor natural (un-cued) swallows. The covert swallowing task was chosen to provide a more precise evaluation of sensorimotor components related to swallowing and to limit ancillary functional activation caused in visual or auditory stimulation that results from cued tasks. Additionally, the natural swallow is shown to have small accompanying motions, limiting motion-related artifacts in the functional imaging results. The aim of the present research was to test the feasibility of using SimulScan to effectively image oropharyngeal structures and functional brain activation during swallowing. The designed pulse sequence is described and a protocol is given describing the acquisition and analysis. Additionally, functional activations from the covert swallowing task are compared to a previously published cued fMRI swallowing task.

2.2. Methods

All data were acquired on a Siemens Magnetom Allegra 3 T head-only scanner equipped with a single channel birdcage head coil. The scanner is capable of a per axis maximum gradient amplitude of 40 mT/m, and slew rates up to 400 mT/m/ms, although limits of 34 mT/m and 250 mT/m/ms were used in the current work. The developed pulse sequence that interleaves the functional and dynamic acquisitions, SimulScan, was used to collect the data. Three healthy young adult volunteer subjects with no history of swallowing disorders were studied in accordance with the protocol approved by the institutional review board of the University of Illinois.

2.2.1. SimulScan Pulse Sequence Design

The SimulScan pulse sequence consists of interleaved dynamic and fMRI acquisition blocks as shown in Figure 3a. A single mid-sagittal slice was used to capture dynamic oropharyngeal swallowing events and 24 oblique axial slices were used to acquire functional slices of the brain. The sequence acquired 1 dynamic

image for every functional slice, as shown in Figure 3b. Both the dynamic and functional portions of the acquisition used a spiral acquisition (28). The dynamic acquisition involved a 6-shot spiral-out FLASH acquisition to image a single 6 mm thick mid-sagittal slice. The parameters used include 240x240 mm FOV, 96x96 matrix, 2.5x2.5 mm resolution, TE 1.1 ms, flip angle of 10° and a TR of 68.8 ms. The resulting dynamic frame rate was 14.5 fps. The fMRI acquisition used a single-shot spiral-in readout to image 24 slices each 4 mm thick, 240x240 mm FOV, 64x64 matrix, 3.75x3.75 mm resolution, TE 25 ms, flip angle of 80° and an effective TR of 1.6512 s.

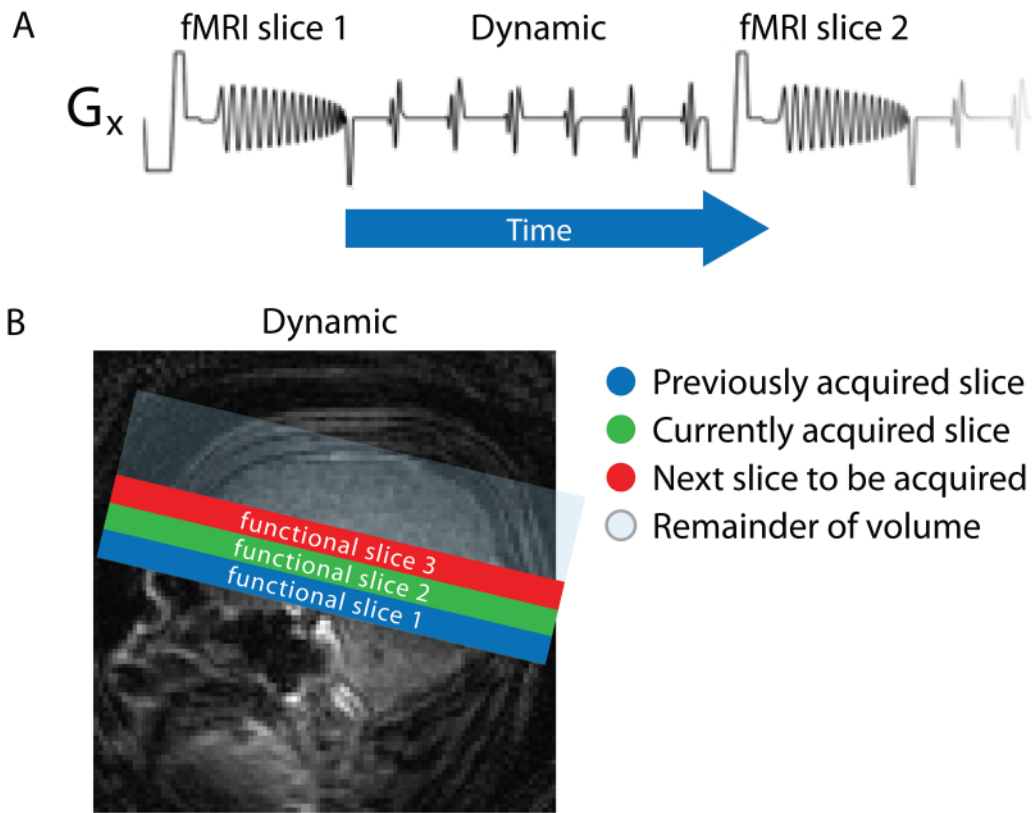


Figure 3. Illustration of (a) gradient in x-direction, G_x , during SimulScan, showing interleaved sequence blocks (b) relative position of dynamic acquisition and functional slice acquisitions.

2.2.2. Task Paradigm

To investigate brain activations associated with natural spontaneous swallowing, a simple covert-swallowing paradigm was employed. The focus of the experiment was not explained to the subject until after the scans were completed. Padding was used in the head coil to restrict subject head motion. Three 15-minute scans were acquired while the subject watched an animated film of their choice. The film was not associated with the swallowing task. The task varies from traditional fMRI paradigms where a stimulus is provided to cue the task. Instead this study examined un-cued swallows. Because swallowing occurs naturally, the imaging sequence was simply made long enough to ensure enough swallows would be observed. Previous research suggested that the subjects would swallow at an average rate of 1.32 spontaneous swallows/minute (29). This would result in approximately 60 swallows over the study with random spacing determined by the subject. The onsets of swallowing events were later determined using the acquired dynamic images of the oropharyngeal region. In addition to the SimulScan sequence, high-resolution proton density- and T2-weighted images were acquired with the functional acquisition slice prescription in addition to a high-resolution 3D structural image using a magnetization-prepared rapid acquisition of gradient echo sequence (MPRAGE).

2.2.3. Data Analysis

Data analysis consisted of four steps: determining the timing of swallow onsets, fMRI analysis, quantifying the contribution of motion and identifying regions of activation. To determine swallow onsets, a rectangular region of interest (ROI) was placed on the sagittal dynamic image in the area including the base of tongue (BOT) and the posterior pharyngeal wall (oropharynx). The ROI was positioned so that contact between the base of the tongue and the oropharynx during swallowing would fall within the ROI and the average intensity within the region would increase (Figure 4a). The peak intensities were a robust indicator of swallowing activity

(Figure 4b), and were similar to timings gathered by visual inspection of the dynamic videos. The detection method required the ROI be small enough so that the intensity increase caused by contact of the base of the tongue to the oropharynx would cause a detectable change in the mean intensity of the ROI, but large enough so that movement variability would not cause the contact point to move outside of the ROI. A ROI of 10 voxels was used. To quantify detection capabilities, the SNR of this signal was found by analyzing the amplitude of the ROI time-series during a swallow versus its baseline standard deviation. The SNR of the swallowing peaks is 18.1, showing that the swallowing events were easy to detect from the time series data. For comparison, a visual inspection of the contact between the base of the tongue and the oropharynx was also used as an indicator of swallowing. The automated timings were used in the subsequent FSL analysis.

Functional MRI data processing was performed using the FMRI Expert Analysis Tool (FEAT) from the FMRIB's Software Library (FSL) (30). Pre-statistics processing steps include motion correction using MCFLIRT (31) and brain extraction using BET (32). A Gaussian kernel was used to smooth using a FWHM of 5.0 mm and a high pass filter of 30 s was applied to the time series of functional MRI data. The computed onset timings were convolved with the canonical hemodynamic response function for use in general linear modeling for each run of each subject. A multi-stage registration and normalization was then performed using the low-resolution T2 image and the high-resolution MPAGE, to match the MNI template. A second-level fixed effects analysis was performed to find the activations of each subject over all runs. And a second higher-level fixed effects analysis was performed to find activation common among all subjects. This was thresholded with a Z threshold of 3.0 and Cluster P threshold of 0.05 to correct for multiple comparisons with Gaussian random field theory (33). Anatomical regions of activation were determined by comparing thresholded functional maps to the Talairach atlas provided in FSL (34).

2.3. Results

2.3.1. Image Quality

The dynamic anatomical images show susceptibility related artifacts. In general these artifacts are not ideal, but the resulting images are sufficient to detect the swallowing motion. Also, both dynamic and functional images show a saturation effect due to the interleaved acquisition. For example, a sagittal dynamic slice will have a saturated band at its intersection with an axial functional slice that was acquired just prior to the dynamic slice (Figure 4a). The axial functional slices also have a saturated band caused by the sagittal dynamic slice.

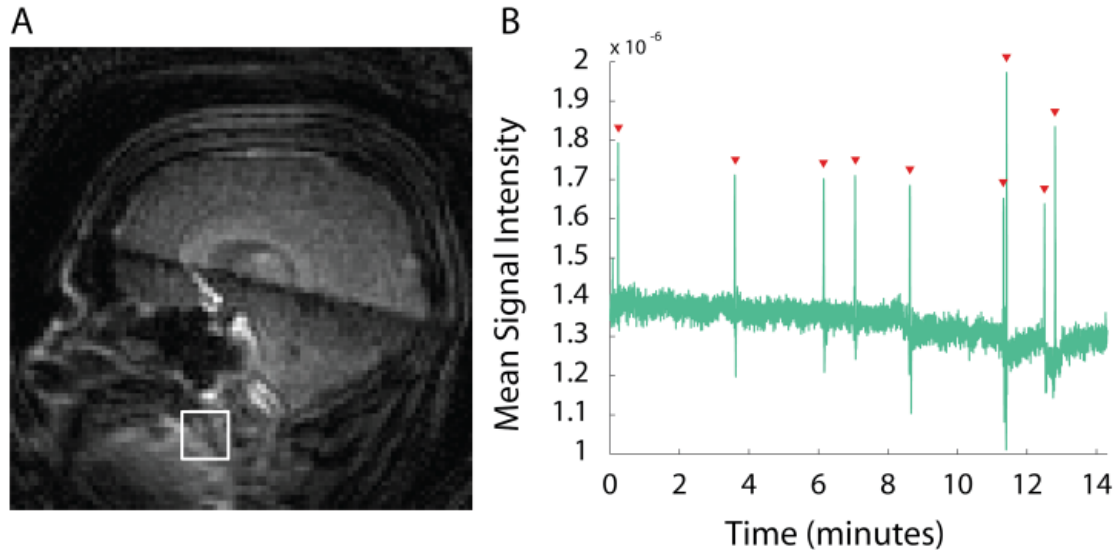


Figure 4. Illustration of ROI analysis used for automated detection of swallowing, (a) ROI is positioned to cover base of the tongue and posterior pharyngeal wall, (b) detected swallows, indicated by marking above peaks.

2.3.2. Number of Swallows

Timings onsets of the swallows were determined from the ROI analysis based on the dynamic images as described in *Data Analysis* and in Figure 4b. Subjects 1, 2, and 3 swallowed on average 8.67, 37.67 and 18.67 times per run (Table 1). Subject 2 had a higher swallowing frequency. Notably this subject reported to have flu-like

symptoms on the day of the experiment, which may be associated to the more frequent swallows.

Table 1: Number of un-cued swallowed detected for each subject.

	Subject 1	Subject 2	Subject 3
Run 1	9	35	30
Run 2	6	36	14
Run 3	11	42	12
Average	8.67	37.67	18.67

2.3.3. Functional Brain Activation and Validation

Results of fMRI data processing show significant activations in sensorimotor regions of the brain (Figure 5). As can be observed, activation was significant in most of the primary motor and somatosensory cortex, as well as in sensorimotor integration areas, such as the thalamus and premotor cortex.

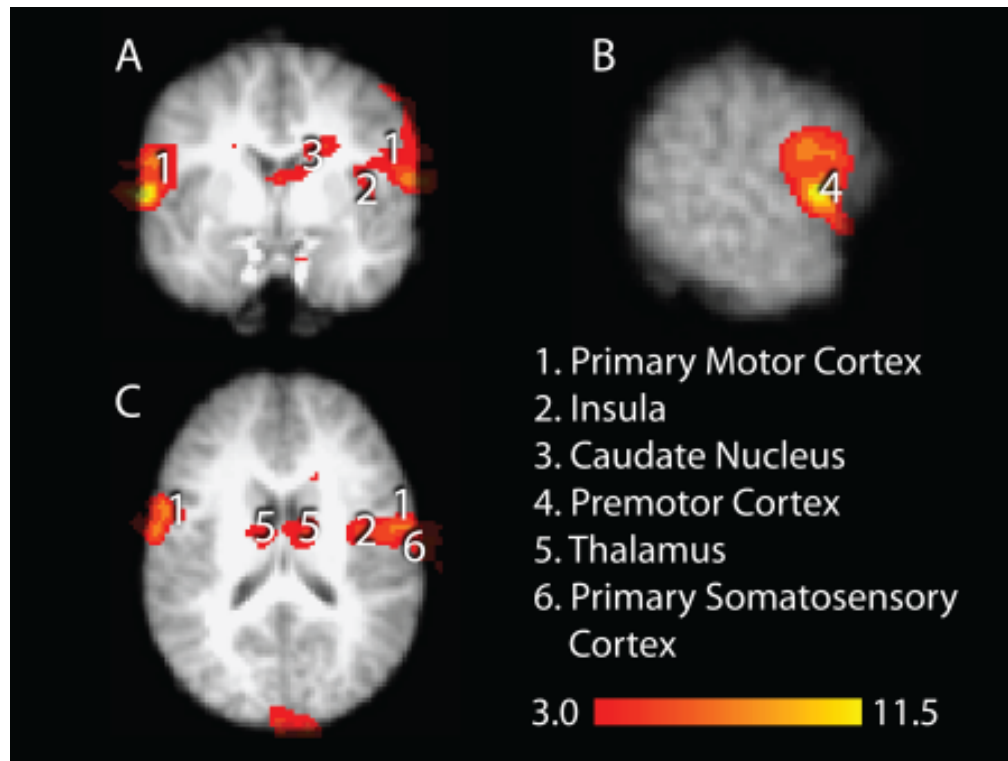


Figure 5. Results of functional analysis in (a) coronal, (b) sagittal, and (c) axial cross-sections.

To validate the functional results detected and to examine how a natural swallow compares to a cued swallow, results of the present experiment were compared to a previous fMRI investigation using a cued swallowing paradigm (10). Table 2 shows the comparison of regions that were found as activated in these two studies. The results show that nearly all of the same areas related to motor control, sensory input and somatosensory integration are significantly activated, though the significant activations from the present study are much more localized to motor control areas.

Table 2: Areas of significant activation during un-cued swallowing found in our current study compared to a previous study of cued water swallowing.

Research Study	Common to Current Study and Cued Water Swallowing (10)	Cued Water Swallowing (10) Only
Areas of activation during swallowing	Primary motor area (precentral gyrus, BA 4) Primary sensory area (post-central gyrus, BA 3) Supplementary motor area and middle and superior frontal gyrus (BAs 6 and 9) Insular cortex (BA 13) Heschl's gyri (BA 42) Superior and inferior parietal lobules Anterior and posterior cingulated gyrus (BAs 24, 30, 31) Thalamus Midbrain Cuneus Cerebellar regions in both the anterior and posterior lobes	BA 8 of frontal cortex Heschl's gyri (BA 41) Precuneus
Visual areas		Extensive Visual processing areas

2.3.4. Motion Analysis

Motion determined by MCFLIRT ranged from 0.04169 mm to 1.0992 mm for translational displacement and 0.0017 rad to 0.0118 rad for rotation among all subjects. The max displacement and rotational motion for subject 1 was 1.0992 mm and 0.0101 rad. Subject 2 showed max translational motion of 0.8664 mm and max rotational motion of 0.0118 rad. Subject 3 showed translation and rotational motion of 0.9639 mm and 0.0100 rad. Although these movements are sub-voxel in size and should cause minimal error in the functional results, if the motion is correlated with the swallows it can provide false activation results. To examine the impact of motion on the fMRI results, we examined activations with and without motion parameters included as regressors in the general linear model. Activations were compared from the two analyses and showed the same areas of activation in each case with similar z-scores in activated regions. Further no correlated gross head motion was observed with visual inspection of the dynamic images of the natural swallows.

2.4. Discussion and Conclusion

The objective of the present work was to develop and validate a pulse sequence capable of simultaneous functional brain imaging and dynamic imaging of the biomechanics of natural oropharyngeal swallows. The results support the feasibility and applicability of the SimulScan technique. All swallowing events for all subjects were successfully detected by automated processing of the dynamic MRI acquisition. Functional MRI, simultaneously acquired, was used to find areas of significant brain activations in regions typically identified as components of the swallowing network. These functional results were validated through comparison to previously published results, showing many of the same areas of activation. To our knowledge, this is the first study documenting simultaneous acquisition of functional MRI and dynamic MRI of swallowing. Apart from improving understanding of the neural control of normal healthy swallowing, this new

technique will enable simultaneous visualization of neural and muscular components of swallowing abnormalities in patients with dysphagia, and thus allowing direct clinical associations between the two components.

The fMRI results showed significant activation in regions commonly identified as swallowing network areas, as shown in previous studies (10). The differences between the two studies, including Brodmann area 8, Brodmann area 41, precuneus (Table 2), and visual areas, may be explained by many factors. The precuneus for instance is known to be associated with visual and tactile cuing (35). The additional areas of activation seen during swallowing in the previous cued water swallowing study may be due to visual processing of the stimulus and additional sensory input in the oral cavity caused by the entrance and presence of the water. It is likely that the present study using SimulScan was able to show the activations related to natural spontaneous swallowing without interference of external oral sensory and visual stimuli. Note that while the present study is natural in the sense that it was not cued, it was performed in a supine orientation. Typical MRI scanners constrain the subject to a supine orientation during imaging. Studies have shown that gravity can have effects on the behavior of muscles involved in speech (29). Swallowing performed in an upright MR scanner may provide images of swallowing free of these gravity driven effects.

In the current research, the dynamic MR images acquired by SimulScan can be used to determine swallowing initiation times, but more sophisticated dynamic information is available in these images. Dynamic MR images can provide more detail of soft tissue structures involved in deglutition than video fluoroscopy, without need for a contrast agent. In future work, oropharyngeal structures could be identified and more clinically-relevant movement parameters could be measured. Note that although this study shows the monitoring of a mid-sagittal slice during swallowing, the sequence allows separate graphical slice prescriptions for the dynamic and functional imaging portions of the sequence. The dynamic slice prescription can be modified to image clinically relevant parameters in any plane for improved monitoring of specific swallowing parameters.

Given that SimulScan achieves imaging rates of 14.5 frames per second, it is not fast enough to fully resolve certain swallowing phenomena such as velar elevation during swallowing that is achieved in approximately 50 ms (25). Higher frame rates are necessary to delineate these motions and the current study can only resolve the endpoints of the motion (21). Since swallows are repeated many times to obtain adequate signal-to-noise from the functional MRI activations, retrospective gating could be used to obtain a higher-quality, average dynamic image of the motion involved (17-36). High frame rates have been achieved in MRI by gating the acquisition. Gated acquisitions do not account for potentially significant variations that can result from something as simple as repeating a single word (17-21). The current study relies on a real-time monitoring of the dynamic events, i.e. un-gated acquisitions. However, these images suffer from several significant tradeoffs: spatial vs. temporal resolution and temporal resolution vs. magnetic susceptibility artifacts. Additional work on optimizing the acquisition and reconstruction may improve some of the current tradeoffs.

A major concern when imaging swallows is motion-induced artifacts. Functional images may be distorted by bulk movement inside the field of view, as well as movement outside the field of view, such as swallowing. Problems may include steady-state signal errors or changes in magnetic susceptibility artifacts (37). To limit motion-induced activation artifacts, some cued swallowing studies use the behavioral interleaved gradient method (38-40). That method has not been employed here. Instead, statistical analysis was performed with and without motion parameters included in the regression model to examine the impact on the functional results from motion during natural swallows. Bulk translational and rotational motions were determined by MCFLIRT (31). Also sagittal dynamic images were observed to examine the extent of bulk motion. No visible motion-induced artifacts are present in the current analysis, either in the functional images, or bulk motion in the dynamic images, which suggests that natural saliva swallows are associated with minor movements.

Besides bulk motion artifacts, which were shown to be minimal, it is possible that variations in the magnetic field in the human brain result from the process of

swallowing. The magnetic susceptibility depends on the orientation of tissue structures with air spaces throughout the head and neck. Motion of the oropharyngeal structures, especially the tongue and jaw, alter the susceptibility-induced magnetic field distribution even at the brain slices being imaged for the fMRI component of the SimulScan sequence. Although not seen in the current data set, artifactual activations could occur in data at or near the base of the brain due to these motion-induced susceptibility changes. Simultaneous field-mapping could be added to the sequence by introducing a slight delay to the data readouts during the dynamic imaging portion of the sequence (41). This would result in obtaining dynamic field map values in the sagittal plane through the brain to monitor changes associated with movements. The penalty for this addition to the sequence would be an increase in the effective TR for both the dynamic and functional portions of the SimulScan sequence.

The proposed technique may prove an essential pre-surgical tool for patients who have to undergo neurosurgery for brain abnormalities and occasionally end up with multiple swallowing difficulties post surgery. This technique may offer important information on individualized neural areas that should be spared during surgery for an intact swallow to occur post surgery. Furthermore, this simultaneous imaging possibility provides the innovative capability to apply and visualize the effects of swallowing treatment techniques (such as head postural adjustments or sensory enhancement techniques) on the oropharyngeal biomechanics and the brain activation at the same time. This has the potential to significantly enhance understanding of the direct effects of swallowing treatments on the oropharyngeal swallowing and on the neural control of swallowing. This may lead to improvement of existing treatment techniques and development of new, individualized and more effective treatment techniques.

3. CALIBRATION TO REMOVE SPATIAL VARIATION IN BOLD RESPONSE FROM SUSCEPTIBILITY GRADIENT

3.1. Introduction

We saw in the previous chapter that fMRI provides a powerful technique to examine brain function, including cognitive, sensory, and motor functions. Magnetic susceptibility provides a window into brain function with the BOLD response. However, macroscopic magnetic susceptibility effects can also disrupt acquisition of accurate functional imaging results, causing function to be mistakenly positioned in the brain or for function to be improperly weighted or missed in an imaging study.

Macroscopic magnetic-field inhomogeneity will lead to several artifacts in functional MRI images, including image distortion, through-plane susceptibility-induced signal loss, and k-space trajectory distortions. The first two artifacts have been extensively studied in the literature and mechanisms have been found to address their effects on fMRI data. For a few early examples see the following papers: (42-47). The third artifact, k-space trajectory distortions, the core of the current study, are caused by in-plane susceptibility gradients.

Local gradients in the magnetic field map will appear to nearby proton spins as an applied magnetic-field gradient in addition to the gradients used to perform spatial encoding. In effect, for each voxel, k-space is transverse along a different trajectory than intended, shifted by the susceptibility gradient during the preparation phase of the imaging experiment and skewed by the susceptibility gradient during the encoding phase. These k-space trajectory distortions have two possible effects: k-space sampling density changes and echo time shifts.

In (48) it was noted that susceptibility-gradients cause signal loss when they shift the k-space trajectory far enough that the k-space center is not sampled. A maximum echo time for gradient echo experiments was determined to achieve sufficient sampling of the signal intensity in a voxel for a given susceptibility

gradient distribution. Non-Cartesian acquisitions such as spiral result in additional sampling issues (49,50). For example, (50) used a conjugate phase reconstruction that compensated for the sample density of shifted and skewed spiral k-space trajectories caused by susceptibility gradients. This compensation largely corrected for residual signal pile-up artifact common to conjugate phase reconstruction.

In addition, local k-space trajectory distortions cause spatially-varying echo times and in the gradient-echo acquisitions commonly used in fMRI spatially-varying BOLD-sensitivity (51). Echo time (TE) is defined as the time from the center of the RF excitation pulse until the center of k-space is sampled. Equivalently, TE is the point in time that the net gradient waveform integrates to zero on all k-space axes. An important design parameter, the TE determines the bulk contrast of an image and modulates the functional weighting in a BOLD acquisition. In (51), susceptibility gradients were analyzed for their effect on a breath hold fMRI study using an EPI readout. Krishnan et al (52), experimentally verified the echo shifting for spiral-in and spiral-out acquisitions. In (53), the authors described the net k-space trajectory from susceptibility gradients in relation to dual spiral-in and dual spiral-out acquisitions. Both of these works report that for spiral-out effective echo times are longer than specified and for spiral-in effective echo times are shorter than specified. Both also noted that altered echo times have consequences for susceptibility-induced signal loss and BOLD sensitivity. Previous techniques have been proposed to address these BOLD sensitivity changes by altering the imaging experiment (51). These however are difficult to implement for fMRI research sites that do not have a dedicated MR physicist, and must be tailored specifically to the acquisition trajectory.

The effect of susceptibility gradients on BOLD sensitivity depends on several MRI acquisition protocol choices: the trajectory, echo time, bandwidth, and phase encode direction. With knowledge of these protocol choices as well as a magnetic-field map, a map of expected BOLD sensitivity values can be determined. This BOLD sensitivity map can be used as a calibration, removing susceptibility-gradient BOLD-sensitivity variations from individual subjects.

In this work, we provide and validate a calibration procedure for BOLD fMRI based on the susceptibility gradients from a magnetic-field mapping scan on a subject. We show that this calibration procedure removes a significant amount of the spatial variance in percent-signal-change measures in ROI's for a breath-hold task.

3.2. Theory

Most fMRI experiments are performed using a gradient echo (GRE) sequence. For GRE fMRI the magnitude of the BOLD signal has a strong dependence on the echo time. The image of the object created by gradient echo imaging experiment is weighted by the T_2^* decay. T_2^* is a decay constant that depends on T_2 , as well as microscopic magnetic-field inhomogeneity, and so is sensitive to BOLD signal changes.

$$i(\vec{r}) = \rho(\vec{r}) \exp(-TE/T_2^*(\vec{r})), \quad (12)$$

In fMRI, the PSC change is used to see the difference in BOLD signal between active, and rest states. This can be stated as

$$PSC(\vec{r}) = \frac{i_{active}(\vec{r}) - i_{rest}(\vec{r})}{i_{rest}(\vec{r})}, \quad (13)$$

Given a particular TE and without susceptibility gradients, the expected percent signal change can be explicitly written as

$$PSC(TE, \vec{r}) = \frac{\exp(-TE/T_{2,active}^*(\vec{r})) - \exp(-TE/T_{2,rest}^*(\vec{r}))}{\exp(-TE/T_{2,rest}^*(\vec{r}))}, \quad (14)$$

where $T_{2,rest}^*$ is the T_2^* relaxation constant during rest, and $T_{2,active}^*$ is the T_2^* relaxation constant during the active state. For the particular echo time and uniform T_2^* differences between rest and activation across the brain, all voxels would demonstrate the same PSC. For the values of $T_{2,rest}^*$ and $T_{2,active}^*$, we used the values for sensorimotor cortex previously reported for 3 T as 48.9 and 49.6 ms, respectively (54). The result of these uniform T_2^* approximation is to make the PSC estimate no longer depend on space and can be given by

$$P\hat{SC} = \frac{\exp(-TE/T_{2,active}^*) - \exp(-TE/T_{2,rest}^*)}{\exp(-TE/T_{2,rest}^*)}, \quad (15)$$

If susceptibility gradients exist, then the k-space trajectory will suffer from shifts and skews, which will change the effective echo time (TE_{eff}), *i.e.* the time at which the effective k-space trajectory crosses the origin. The equation for TE_{eff} can be generally expressed as

$$TE_{eff}(\vec{r}) = \arg \min_{t_n} \left(\sqrt{(k_{x,n} + G_{susc,x}(\vec{r}) \cdot FOV \cdot t_n)^2 + (k_{y,n} + G_{susc,y}(\vec{r}) \cdot FOV \cdot t_n)^2} \right) + t_{prep}, \quad (16)$$

Where, $k_{x,n}$ and $k_{y,n}$ are the k-space coordinates, $G_{susc,x}$ and $G_{susc,y}$ are the susceptibility induced gradients in the x- and y-direction at a given voxel location. The sample time is t_n and t_{prep} is the time from the center of the RF excitation to the start of sampling. Figure 6 helps illustrate this

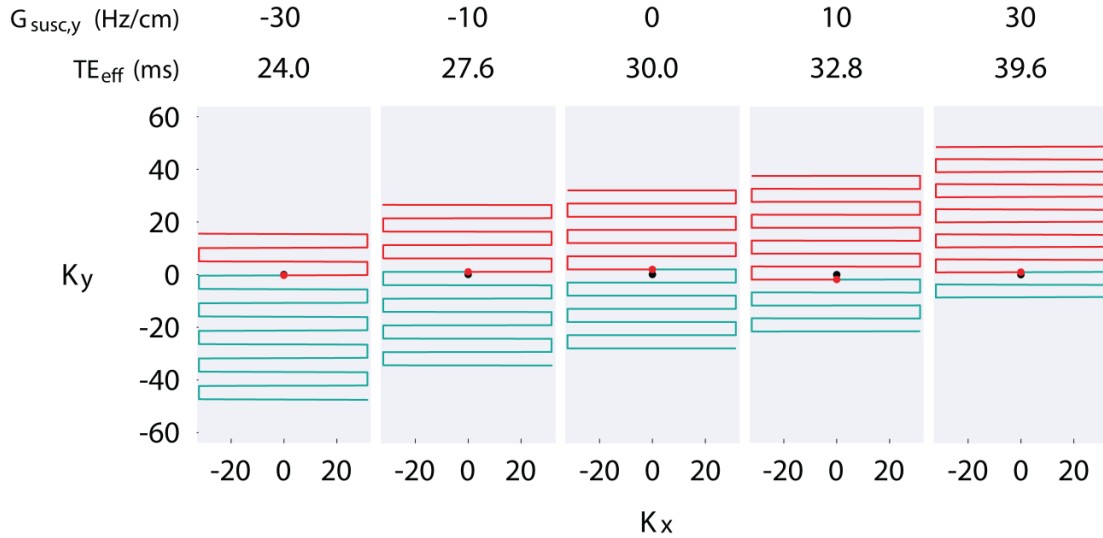


Figure 6. Illustration of susceptibility gradient affects on a Cartesian k-space sampling trajectory. Note the center of k-space. The red line descending from the top of the trajectory are the samples acquired before sampling the center of k-space. A longer red line is related to a longer effective echo time.

The trajectory is composed of a fixed number of sampled. A negative susceptibility gradient shifts the effective trajectory down, and stretches it. This causes the center of k-space to be sampled sooner (shown by overlapping red dot, the sample nearest the center of k-space, and black dot, actual k-space center). Each

sample point is related to a sample time, and this is used to calculate the effective echo-time.

The effects of susceptibility gradients on BOLD sensitivity were examined by Deichmann and colleagues in (51), and we follow the same logic in this work. We will denote the effective TE as TE_{eff} . Using this TE_{eff} , Equation 14 becomes,

$$P\hat{S}C_{eff}(\vec{r}) = \frac{\exp(-TE_{eff}(\vec{r})/T_{2,active}^*) - \exp(-TE_{eff}(\vec{r})/T_{2,rest}^*)}{\exp(-TE_{eff}(\vec{r})/T_{2,rest}^*)}, \quad (17)$$

Note that this effective PSC depends on the effective echo time for each voxel. TE_{eff} is found by simulating the applied imaging trajectory along with the in-plane susceptibility gradients to determine the effective k-space trajectory and effective echo time for each voxel. We can form the ratio between Equations 17 and 15 to determine the anticipated scaling of the BOLD response due to echo shifting. This is our calibration map $Cal(r)$, which is given by,

$$\hat{C}al(\vec{r}) = \frac{P\hat{S}C_{eff}(\vec{r})}{P\hat{S}C}, \quad (18)$$

The calibration map, $Cal(r)$, describes the scaling of the sensitivity to the BOLD activation due to the echo time shifting from the susceptibility gradients, with TE_{eff} a function of the spatial susceptibility gradients at a position (x,y) . Calculation of the TE_{eff} for a particular voxel requires consideration of the susceptibility gradients, the imaging k-space trajectory, acquisition timing, and the choice of phase encode direction.

By dividing the experimentally measured PSC by the calibration map, PSC values can be obtained that are not dependent on the susceptibility gradients, removing the spatial variability in BOLD data. It is expected that this calibration will remove spatial variability in the percent signal change response that results due to distributions of susceptibility gradients, especially in inferior brain regions.

3.3. Methods

3.3.1. Task Paradigm

Our goal is to develop a calibration technique that can remove the spatially-varying BOLD sensitivity effect, caused by in-plane susceptibility gradients. To test this, we first must observe uniform whole-brain BOLD activation. This is approximated by having subjects perform a hypercapnic or breath hold (BH) task (55). When the brain is briefly deprived of oxygen it results in a BOLD-like response that only varies due to local vasculature differences. This breath hold challenge has been examined as a means to calibrate BOLD signals both spatially and across subjects (55,56). Subjects were visually cued to perform a block task of end-inspiration breath holding. Seven blocks of 18 s of free breathing (“rest”) with 18 s of visually cued breath holding (“task”) were performed. During the task, the visual cues instructed subjects to “Take a deep breath and Hold”, followed by a counter that indicated progression through the breath hold interval. All subjects were able to complete the task. Subject motion was minimized through a practice session and the use of padding.

3.3.2. Data Acquisition

Subjects were scanned in accordance with the Institutional Review Board of the University of Illinois at Urbana-Champaign. Twenty-eight healthy adults subjects participated in the study, including fourteen young adults (19-32 years old, mean age 25, 8 females) and fourteen old adults (61-72 years old, mean age 66, 7 females), although the current study does not include an analysis of age or gender. This study was conducted in conjunction with a separate study on visual discrimination and aging (57). Subject scans were performed using a Siemens (Erlangen, Germany) Allegra 3 T MRI scanner. Magnetic field maps were acquired with the vendor-supplied multi-echo gradient echo sequence with the following parameters: TE =

4.89, 7.35 ms, TR = 390 ms, field of view = 24 cm, matrix size = 64x64, 32 slices 4 mm thick, oblique-axial scans aligned to AC-PC.

One aspect of the study was to observe how different k-space sampling trajectories affected the spatially-varying BOLD effects. Consideration of the exact sampling trajectory for the experiment is necessary in order to accurately combine imaging and susceptibility gradients into an effective k-space trajectory. The k-space trajectories considered were echo planar imaging (EPI) with phase encoding the anterior/posterior direction (EPI-down) and EPI in the posterior/anterior direction (EPI-up) as well as two variants of a spiral acquisition, one starting at the center of k-space and sampling outward (Spiral-out), and another starting at the edge of k-space and sampling inward (Spiral-in). Within a chosen sampling trajectory, there are many differences in imaging protocols that can have a significant effect on the impact of susceptibility gradients. For example, for EPI trajectories, these protocol differences include: ramp sampling, gradient performance, slice orientation, echo spacing, and the quality of the magnetic field shimming procedure, among others. All sequences examined in this study had a common echo time of 30 ms. The EPI sequences had an echo spacing of 0.4 ms and a matrix size of 64x64, typical of EPI sequences at our site. Thirty-two slices 4 mm thick with a 10% gap between slices were acquired with a field of view of 22. With these parameters fixed, the impact of susceptibility gradients on the EPI sequence mainly depends on the phase-encode direction. The spiral-in and spiral-out sequences that were examined also used a matrix size of 64x64. The spiral was designed using the analytic expressions found in (28), with a maximum imaging gradient amplitude of 20 mT/m and a maximum slew rate of 200 mT/m/ms.

Two main studies were performed. In the first study, a single subject performed the BH task for each of the four k-space trajectories previously mentioned. Field maps were obtained, and effective PSC maps were calculated by determining the TE shifts due to susceptibility gradients for each trajectory. These effective PSC maps were compared to experimentally measured PSC maps. In the second study, 27 subjects performed the BH fMRI task. An EPI up trajectory was used for functional imaging. Again, field maps were obtained for each subject, and

effective PSC maps calculated. For this study, calibration was also performed and analyzed.

Magnetic field maps were acquired with the vendor-supplied multi-echo gradient echo sequence with the following parameters: TE = 4.89, 7.35 ms, TR = 390 ms, field of view = 24 cm, matrix size = 64x64, 32 slices 4 mm thick, oblique-axial scans aligned to AC-PC.

3.3.3. Calculating Susceptibility Gradients

Field maps were converted to Hz by dividing the difference in phase between the images at the two echo times by the difference in echo time, as

$$\Delta\omega(\vec{r}) = - \frac{\angle i_2(\vec{r}) - \angle i_1(\vec{r})}{2\pi\Delta TE}, \quad (19)$$

where $\Delta\omega(r)$ is the field map in Hz, $i_1(r)$ is the image at TE₁, $i_2(r)$ is the image at TE₂, and \angle indicates that the phase angle of the images were used to calculate the field map. Gradients of the field map are taken by a centered differences in the direction of the positive axis, i.e., as:

$$G_{sus,c,x}(x, y, z) = \frac{\Delta\omega(x + \Delta x, y, z) - \Delta\omega(x - \Delta x, y, z)}{2\Delta x}, \quad (20)$$

for a voxel at position (x,y,z) with voxel size of Δx in the x-direction. The gradients of the field map were calculated in Hz/cm. Given that the field maps are fairly smooth, this differencing method is expected to give accurate estimates of the field map gradients. Higher resolution field map acquisitions could be used to get more localized estimates of the susceptibility gradients which may lead to better estimates of the gradients in regions where curvature of the field map is high. After calculating the susceptibility gradients, the field map and gradient maps were normalized to standard MNI space using FLIRT in FSL (58,59). Further calibration calculations were performed in standard MNI space.

3.3.4. Model Based Estimation of BOLD Sensitivity

The in-plane (x- and y-directed) susceptibility gradients were used to calculate effective k-space trajectories for every voxel based on the applied k-space trajectory and the additional encoding due to the susceptibility gradients at the chosen echo time, by finding the time point when the k-space trajectory was closest to zero, as in Equation 16. This effective echo time was mapped to BOLD sensitivity through the relationship between percent signal change and effective echo time shown in Equation 17. The resulting BOLD sensitivity map showed the BOLD signal at each voxel relative to the predicted BOLD signal based on the nominal echo time. Voxels were discarded from analysis if the net trajectory (imaging plus susceptibility gradients) predicted that the center of k-space was not sampled.

3.3.5. Calibration Analysis

For the twenty-eight subject calibration study, analysis was performed using FMRIB's Software Library (FSL, www.fmrib.ox.ac.uk/fsl). Motion correction was performed on the EPI time series using MCFLIRT (59) and spatial smoothing was performed using a Gaussian kernel of 5 mm. Statistical analysis was performed on the breath hold task (60) and the individual subject results were normalized to the standard MNI template. This normalization produced the experimentally measured PSC map for each subject in a common reference frame for further analysis. The normalization parameters were also applied to the field map images, and propagated to the effective PSC maps. A calibration map was calculated for each subject by forming a ratio between the effective PSC and the nominal PSC estimate given by Equation 15. This ratio is shown in Equation 18.

We focused our analysis for calibration on the temporal lobe as identified by the MNI structural atlas in FSL (61, 62). Inside the temporal lobe, we identified three regions of interest (ROIs) by finding all voxels for which the susceptibility gradient in the phase encode direction (G_y^{SUSC}) was within a certain range. For ROI 1, we used -30 Hz/cm to -10 Hz/cm. For ROI 2, we used -5 Hz/cm to 5 Hz/cm. And for ROI 3, we

used 10 Hz/cm to 30 Hz/cm. Percent signal change (PSC) in these regions of interest was found by dividing the magnitude of the activation regressor by the mean functional image, approximating Equation 13 by Equation 11. For calibration, the PSC map was divided by the calibration map as in Equation 18, before calculation of the ROI mean and standard deviation. An ANOVA analysis was performed on the PSC data from all subjects in ROI 1 and 3 both before and after calibration. We excluded ROI 2, because it has the largest spatial extent, and is more likely to be effected by vasculature differences.

3.4. Results

3.4.1. Analysis of Model

3.4.1.1 Susceptibility-induced magnetic field and gradient maps

A multi-echo gradient echo sequence was acquired and processed to yield magnetic susceptibility gradients. The magnetic field and gradient maps are shown in Figure 7 for a single subject in axial, coronal, and sagittal slices through the orbitofrontal cortex. The magnetic field map has values in the orbital frontal cortex that exceed 100 Hz in the slice shown. The gradients of the field map in the x-, y-, and z-directions reach approximately ± 80 Hz/cm. The sign of the susceptibility gradient is important as it relates to the sign of the applied imaging gradient and the net traversal through k-space. The gradients have been defined as positive from left to right (X-direction) and from posterior to anterior (Y-direction), corresponding to the positive gradient axes for the imaging sequences.

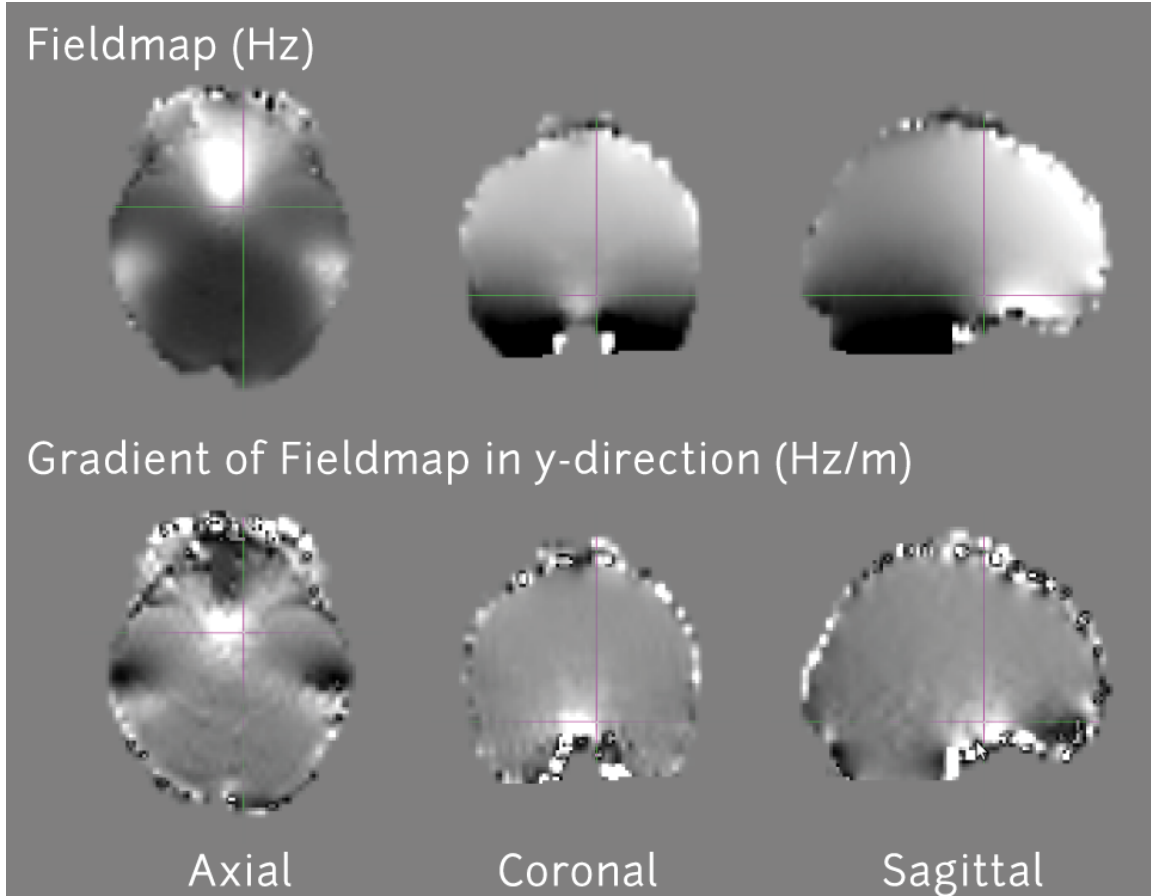


Figure 7. Fieldmap and gradients in the y-direction for a typical subject.

3.4.1.2. Interactions of susceptibility gradients and BOLD sensitivity

Consideration of the sampling trajectory and timing is necessary in order to determine the exact effect of susceptibility gradients on the BOLD signal. This can be seen by examining the predicted echo time shift due to ranges of susceptibility gradients in different directions. In Figure 8, the expected echo time shifts for four example trajectories are displayed with x-axis being the susceptibility gradient in the x-direction and the y-axis being the susceptibility gradient in the y-direction. The k-space trajectories considered were common for fMRI sequences: EPI with phase encode direction anterior-to-posterior (EPI down), EPI with phase encode direction posterior-to-anterior (EPI up), and two variants of a spiral acquisition, spiral-out and spiral-in. All sequences were designed with an echo time of 30 ms and a matrix size of 64 in a 22 cm field of view. The EPI sequence had an echo

spacing of 0.4 ms and the spiral sequences were designed according to (28) with a maximum gradient amplitude of 20 mT/m and a maximum slew rate of 200 mT/m/ms. As can be seen in Figure 8, the sampling pattern and direction of that the trajectory is traversed can have a significant impact on the echo time shifts, and hence the BOLD sensitivity. Remarkably, for the spiral-out acquisition, a susceptibility gradient outside of the range ± 30 Hz/cm results in a shift of the trajectory far enough that the center of k -space is never sampled. In these cases, there is no defined echo time and the signal will become unreliable due to the lack of sampling the center of k -space, *i.e.* the high-signal, contrast-containing region of k -space.

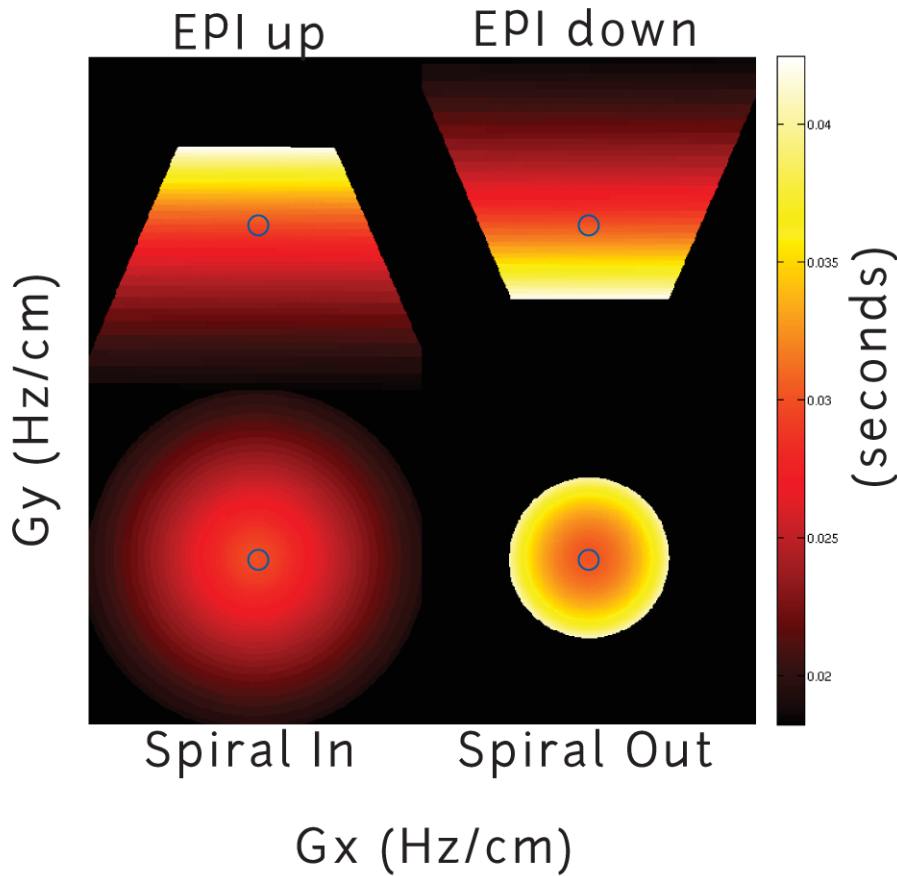


Figure 8. Effective echo time vs susceptibility gradient in the y- and x-direction. Susceptibility gradients values range from -80 to 80 Hz/cm.

These echo time shifts will result in changes in the BOLD signal. When the effective echo times are input into Equation 17 and Equation 18, the resulting calibration maps, $\text{Cal}(r)$, for a typical subject appear as in Figure 9. The calibration map is displayed after normalization to the standard MNI space. The z-values correspond to the slice location in mm in the standard MNI image as viewed in FMRIB's Software Library (FSL, www.fmrib.ox.ac.uk/fsl). Regions that resulted in effective k-space trajectories that do not sample the center of k-space are denoted by a lack of color overlay. In these regions, the BOLD sensitivity is zero and no functional results should be expected from these regions.

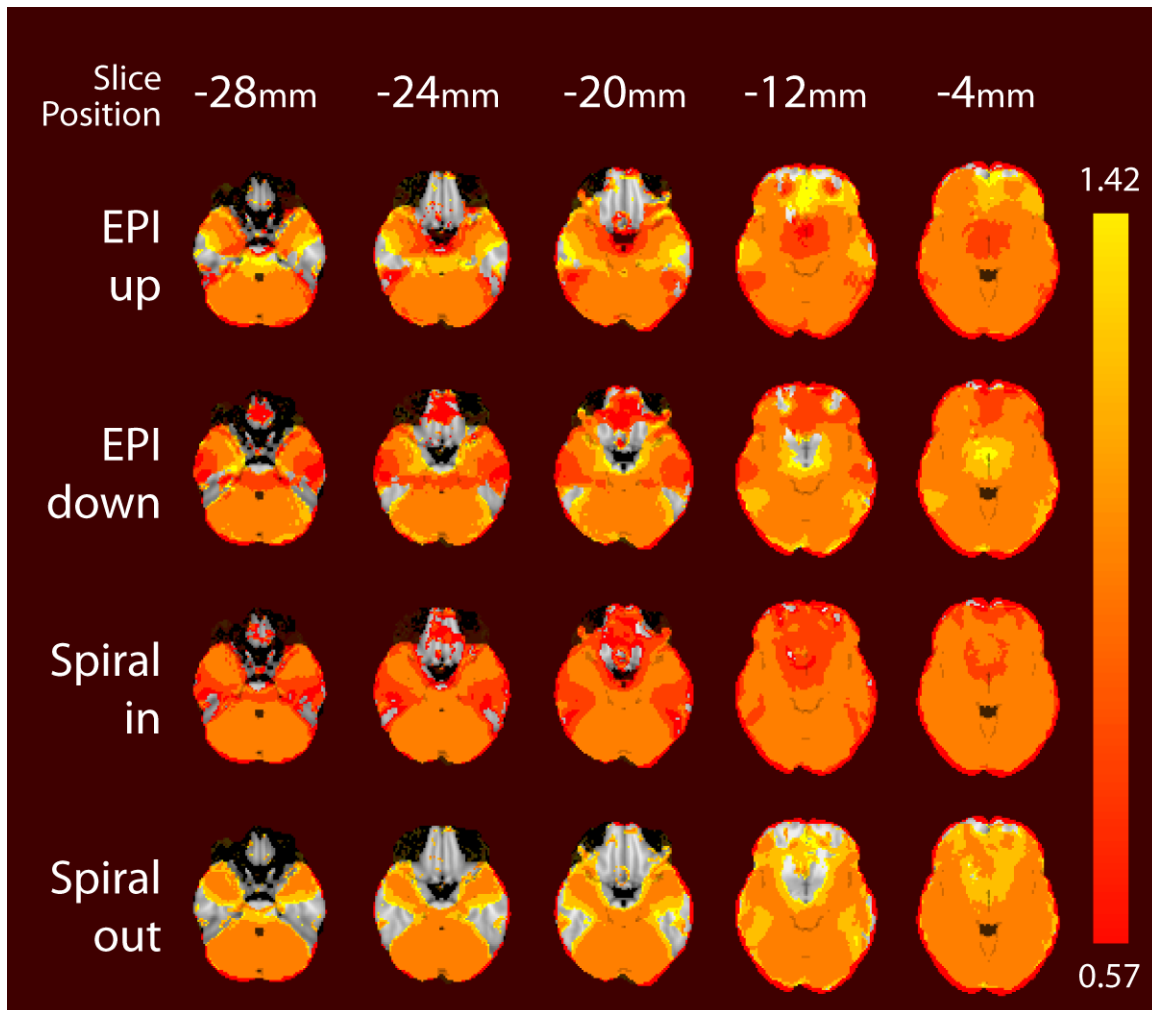


Figure 9. Calibration maps, $\text{Cal}(r)$, for a typical subject for each of the four studied k-space sampling trajectories.

3.4.2. Study 1

The Calibration maps show large regions with no BOLD sensitivity, on the ventral side of the brain, especially in the frontal and temporal lobes. These regions correspond well with the actual BH task PSC results (Figure 10). Specifically areas with no BOLD sensitivity may have Z stat values that do not reach significance. Areas of lowered percent signal change due to echo time shift around -30% and 30% are also shown in the Calibration maps, through these are harder to interpret. While the BH task is expected to provide near global activation, these activations are not expected to be uniform throughout the brain, but dependent on local vasculature responses. Spatial smoothing during FSL analysis (2 mm) and registration to MNI space may have affected the spatial extent of the Z stat maps, as well.

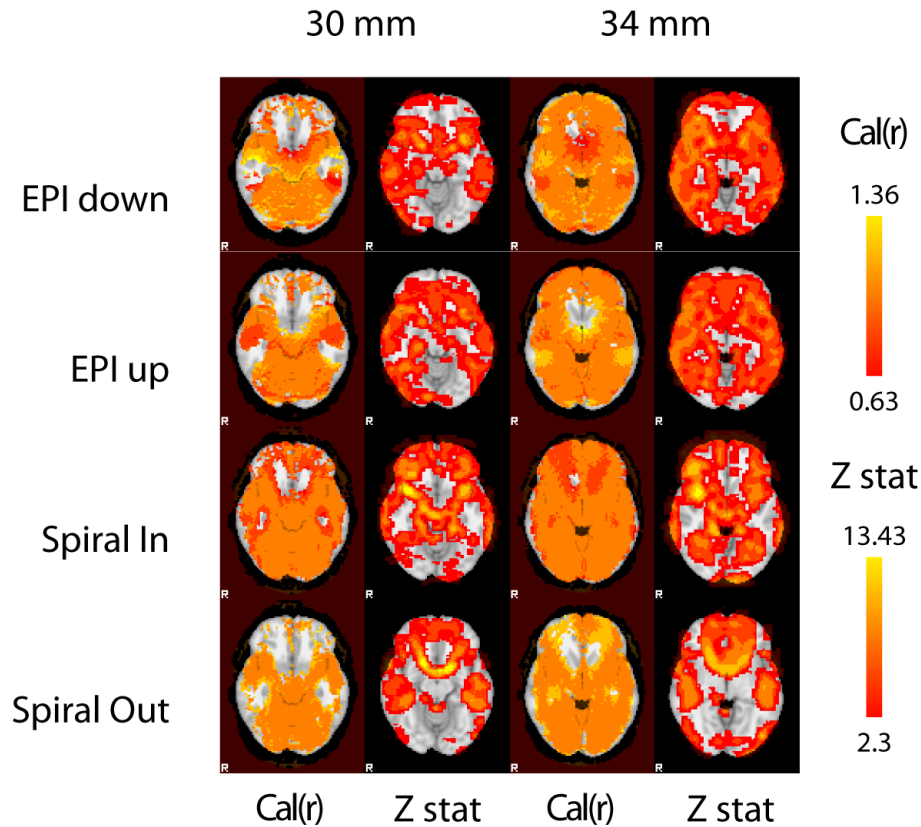


Figure 10. PSCRatio and measured PSC maps for two different slice positions (z=30 mm, z=43 mm) and for 4 trajectories, EPI down, EPI up, Spiral In and Spiral Out.

In the Calibration maps, grey regions represent voxels that failed to capture the center of k-space and have no BOLD contrast. They are expected to correspond to

grey regions in the Z stat that are insignificant. Note that regions with no BOLD contrast and no significant Z stats tend to relate. More importantly, Z stat shows significantly different activation between the four trajectories, as is predicted.

3.4.3. Study 2

3.4.3.1. Calibration of Breath Hold BOLD Signal

Within the temporal lobe, three regions of interest in MNI standard space were defined for each subject, ROI 1: regions having a phase-encode direction susceptibility gradient of -30 to -10 Hz/cm, ROI 2: -5 to 5 Hz/cm, and ROI 3: 10 to 30 Hz/cm. To demonstrate consistent alignment of these subject-defined ROIs, regions in ROI 1 were labeled red, ROI 2 labeled green, and ROI 3 labeled blue. Maps from each subject were added together and divided by the number of subjects, forming a fractional color map (or hit map) for each region, as shown in Figure 11. The map demonstrates that the structural air/tissue interfaces create reliable regions of similar magnitude susceptibility gradients between subjects.

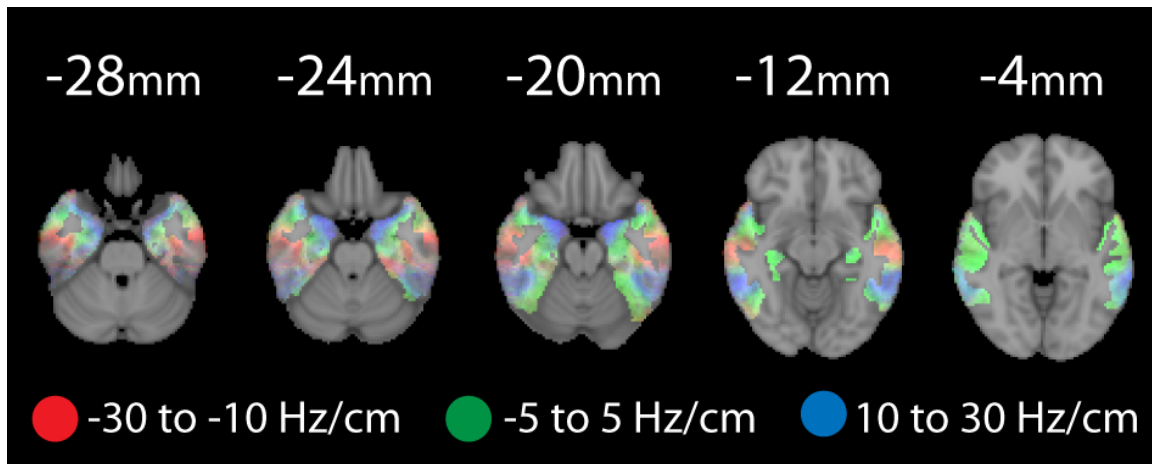


Figure 11. Hit map showing ROI distribution across subjects. A more saturated color in a given voxel means it was present for that ROI in more subjects. Shows that ROI distributions were fairly stable across subjects.

BOLD signals in the form of PSC were extracted from each subject as described in the Methods section both before and after calibration. To determine the relationship between the susceptibility gradient in the phase encode direction and the PSC (both before and after calibration), we performed a regression analysis. For

each subject, we extracted the PSC values in ROI 1 and 3 (-30 Hz/cm to -10 Hz/cm susceptibility gradient in the phase encode direction and 10 Hz/cm to 30 Hz/cm, respectively). An ANOVA analysis was performed on the data before and after calibration. Because the PSC is expected increase nearly linearly as a function of the susceptibility gradient in the y-direction before calibration, the means of the two described ROIs should be different (Figure 12). Ideal, after calibration, the PSC should no longer be a function of the susceptibility gradient in the y-direction, and the means of the two ROIs should be the same. The ANOVA analysis technique was choose because the spatial extent of ROI 2 meant vascular differences played a larger role, and increased the standard deviation. ROI 1 and 3 however were less affected by vascular differences.

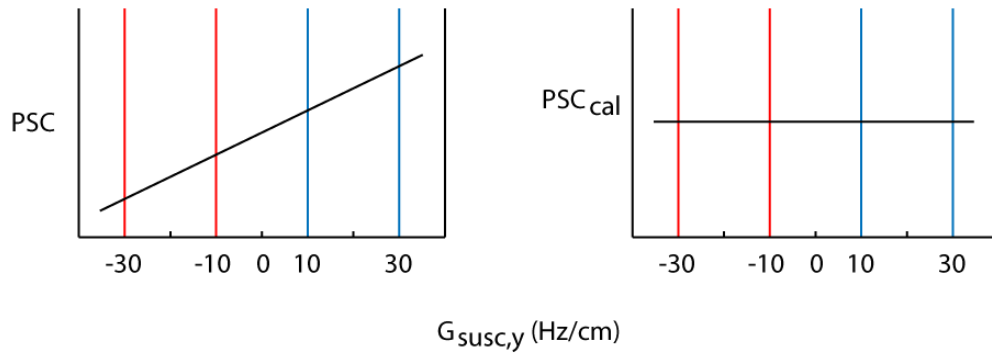


Figure 12. Diagram depicting the ANOVA analysis before and after calibration. Note that this diagram represents the ideal case, and not actual data.

We also calculated the mean of the PSC for each ROI for each subject resulting in values in the uncalibrated data of ROI1: 0.89 ± 0.46 % and ROI2: 1.13 ± 0.56 %. This shows that the ROIs have different mean BOLD signals. The ROI explains a large portion of the variance with an ANOVA analysis resulting in F-test = 9.84, $\eta^2 = 0.05$. For the calibrated data, the means between the ROIs become much more consistent, ROI1: 0.99 ± 0.54 % and ROI2: 1.00 ± 0.56 %. After calibration, ROI differences explain an insignificant proportion of the variance with an ANOVA analysis resulting in F-test = 0.005, $\eta^2 = 3 \times 10^{-5}$.

3.5. Discussion

There are two important results from analyzing the impact of in-plane susceptibility gradients on the functional MRI image acquisition: 1) the determination of spatially-varying BOLD sensitivity and 2) identification of areas that were not adequately sampled due to the net spatial encoding. Both of these effects can have a significant impact on functional MRI studies, as well as the recent field of functional connectivity mapping. We have shown that with a measure of the magnetic field distribution, spatial distribution of BOLD sensitivity due to magnetic field gradients can be predicted and calibrated.

The impact of the susceptibility gradients on effective echo times depends on several factors: the acquisition trajectory used in acquiring data, the echo time chosen for the scan, slice orientation, subject orientation relative to the main magnetic field, quality of the magnetic field shimming procedure, and subject-specific anatomy of air/tissue interfaces. Given the wide variety of protocols and sequences currently in use for fMRI, the impact of these choices on functional imaging data must be made clear. Studies must begin to acquire magnetic field maps with their functional data to allow for assessment of the impact of susceptibility gradients both across studies and across subjects within a study.

Some regions of the orbitofrontal cortex suffer from reduced or lost BOLD sensitivity in all four of the acquisition schemes examined, as shown in Figure 9. Depending on the specific region of interest, an fMRI researcher may choose a particular acquisition sequence based on the expected maximum BOLD sensitivity in the region. Alternatively, changing several other parameters could result in recovery of BOLD sensitivity in these regions for all sequences, including: shortening the echo time, changing the slice prescription, altering the head orientation, or changing the shimming procedure. In future work, we will examine how these parameters affect BOLD sensitivity.

In-plane magnetic susceptibility gradients are often highly correlated with regions of large field inhomogeneity and regions with high through-plane gradients.

These additional effects can be very significant and can dominate or mask the loss of BOLD sensitivity due to the in-plane gradients. Several remedies are available for dealing with image distortion and through-plane signal loss in functional MRI acquisitions. Steps must be taken to ensure that each of these susceptibility effects have been controlled and corrected in the image reconstruction. The current work focuses on the in-plane gradients and the results would be expected to hold if magnetic-field-corrected image reconstructions were performed on thin functional imaging slices to reduce the effects of distortion and susceptibility-induced signal loss, respectively.

For determining the gradients in the magnetic field map in each direction, we used a first-order difference operation in the positive direction of the gradient, as in (60). We expect that the field maps are smooth and that this operator results in fairly accurate measures of the linear susceptibility gradients within an imaging voxel. However, higher resolution field map acquisitions could be used to get more localized estimates of the susceptibility gradients, with spatial derivatives occurring within an imaging voxel. This higher spatial resolution field map may lead to better estimates of the gradients in regions where curvature of the field map is high.

For calibration for approximating the nominal PSC map, we used values of $T_{2,\text{rest}}^*$ and $T_{2,\text{active}}^*$ of 48.9 and 49.6 ms, respectively, as previously reported for sensorimotor cortex (54). One concern might be that these values may differ in different regions of the motor cortex and for different levels of activation of the BOLD hemodynamic response. We investigated the linearity of the calibration over several values of changes in activation level as $\Delta T_2^* = \Delta T_{2,\text{active}}^* - \Delta T_{2,\text{rest}}^*$. We found that the linearity of calibration was well maintained for values up to levels that would result in 10% signal change, well beyond that observable in fMRI experiments. Still, an approximation of the nominal PSC map that allows variation of $T_{2,\text{rest}}^*$ and $T_{2,\text{active}}^*$ over space will be closer to the actually PSC map expressed in Equation 14 should improve over the approximation made in Equation 15.

The analysis of in-plane magnetic susceptibility gradients that is presented here only examines the linear terms in the gradients, as this provides the most direct

relationship to imaging requirements. The magnetic susceptibility maps, however, have higher-order terms and these terms can have significant effects on the images reconstructed. Higher-order gradients within a voxel will result in signal dephasing and perhaps other effects that may be recovered using non-linear encoding schemes that are being developed for imaging applications (63-65).

3.6. Conclusion

Magnetic susceptibility due to air/tissue interfaces results in many artifacts for functional neuroimaging studies that use gradient echo BOLD acquisitions. Although techniques exist to address image distortion and through-plane susceptibility-induced dephasing, the effect of in-plane susceptibility gradients on BOLD sensitivity has not been fully appreciated nor examined. In this study, we showed that knowledge of in-plane gradients in the magnetic field distribution can be used to calculate a calibration map that removes spatial variation in sensitivity in the BOLD response in percent signal change measures. The impact of these sensitivity variations on a functional MRI study can be examined in relation to choices in acquisition trajectory, timing, and subject positioning.

REFERENCES

1. Meyer CH, Hu BS, Nishimura DG, Macovski A. Fast Spiral Coronary Artery Imaging. *Magn Reson Med* 1992; 28*2):202-13.
2. Hoge RD, Kwan RKS, Pike GB. Density compensation functions for spiral MRI. *Magn Reson Med* 1997; 38:117-128.
3. Pipe JG, Menon P. Sampling density compensation in MRI: Rationale and an iterative numerical solution. *Magn Reson Med* 1999; 41:179-186.
4. Jackson JI, Meyer CH, Nishimura DG, Macovski A. Selection of a convolution function for Fourier inversion using gridding. *IEEE Trans Med Imag* 1991; 10(3):473-478.
5. Sedarat H, Nishimura DG. On the optimality of the gridding reconstruction algorithm. *IEEE Trans Med Imag* 2000; 19(4):306-317.
6. Thomas B, Welch E. High-resolution 7T MRI of the human hippocampus in vivo. *Journal of Magnetic Resonance Imaging* 2008; 28:1266-72.
7. Rosen BR, Buckner RL, Dale AM. Event related fMRI: Past, present, and future. *Proc Natl Acad Sci USA* 1998; 95:773-89.
8. Buckner R. Event-related fMRI and the hemodynamic response. *Human brain mapping* 1998; 6:373-77.
9. Ney DM, Weiss JM, Kind AJH, Robbins J. Senescent Swallowing: Impact, Strategies, and Interventions. *Nutr Clin Pract* 2009;24(3):395-413.
10. Malandraki GA, Sutton B, Perlman AL, Karampinos DC, Conway C. Neural activation of swallowing and swallowing-related tasks in healthy young adults: an attempt to separate the components of deglutition. *Hum Brain Mapp* 2009;30(10):3209-3226.
11. Hamdy S, Mikulis DJ, Crawley A, Xue S, Lau H, Henry S, Diamant NE. Cortical activation during human volitional swallowing: an event-related fMRI study. *Am J Physiol Gastrointest Liver Physiol* 1999;277(1):G219-225.
12. Kern MK, Jaradeh S, Arndorfer RC, Shaker R. Cerebral cortical representation of reflexive and volitional swallowing in humans. *Am J Physiol Gastrointest Liver Physiol* 2001;280(3):G354-G360.
13. Martin R, Goodyear B, Gati J, Menon R. Cerebral cortical representation of automatic and volitional swallowing in humans. *J Neurophysiol* 2001;85(2):938.
14. Mosier KM, Liu WC, Maldjian JA, Shah R, Modi B. Lateralization of cortical function in swallowing: a functional MR imaging study. *AJNR American journal of neuroradiology* 1999;20(8):1520-1526.
15. Wein B, Drobnitzky M, Klajman S, Angerstein W. Evaluation of functional positions of tongue and soft palate with MR imaging: initial clinical results. *J Magn Reson Imaging* 1991;1(3):381-383.
16. Shellock F, Schatz C, Julien P, Silverman J, Steinberg F, Foo T, Hopp M, Westbrook P. Dynamic study of the upper airway with ultrafast spoiled GRASS MR imaging. *J Magn Reson Imaging* 1992;2(1):103-107.

17. NessAiver MS, Stone M, Parthasarathy V, Kahana Y, Paritsky A, Paritsky A. Recording high quality speech during tagged cine-MRI studies using a fiber optic microphone. *J Magn Reson Imaging* 2006;23(1):92-97.
18. Inoue M, Ono T, Honda E, Kurabayashi T, Ohyama K. Application of magnetic resonance imaging movie to assess articulatory movement. *Orthod Craniofac Res* 2006;9:157-162.
19. Honda Y, Hata N. Dynamic imaging of swallowing in a seated position using open-configuration MRI. *J Magn Reson Imaging* 2007;26(1):172-176.
20. Breyer T, Echternach M, Arndt S, Richter B, Speck O, Schumacher M, Markl M. Dynamic magnetic resonance imaging of swallowing and laryngeal motion using parallel imaging at 3 T. *Magn Reson Imaging* 2009;27(1):48-54.
21. Sutton B, Conway C, Bae Y, Brinegar C, Liang Z-P, Kuehn DP. Dynamic imaging of speech and swallowing with MRI. *Conf Proc IEEE Eng Med Biol Soc* 2009;2009:6651-6654.
22. Sutton BP, Conway CA, Bae Y, Seethamraju R, Kuehn DP. Faster dynamic imaging of speech with field inhomogeneity corrected spiral fast low angle shot (FLASH) at 3 T. *J Magn Reson Imaging* 2010;32(5):1228-1237.
23. Daniels S. Swallowing apraxia: A disorder of the praxis system? *Dysphagia* 2000.
24. Logemann JA. Evaluation and Treatment of Swallowing Disorders. *Am J Speech Lang Pathol* 1994;3(3):41-44.
25. Kendall K, McKenzie S, Leonard R, Gonçalves M, Walker A. Timing of events in normal swallowing: a videofluoroscopic study. *Dysphagia* 2000;15(2):74-83.
26. Ogawa S, Lee TM, Kay AR, Tank DW. Brain magnetic resonance imaging with contrast dependent on blood oxygenation. *Proc Natl Acad Sci USA* 1990;87(24):9868-9872.
27. Sutton B, Conway CA, Kuehn DP. Simultaneous monitoring of tongue tip movements in functional MRI motor tasks for speech and swallowing studies. *Conf Proc Intl Soc Magn Reson Med* 2009:20.
28. Glover GH. Simple analytic spiral K-space algorithm. *Magn Reson Med* 1999;42(2):412-415.
29. Afkari S. Measuring Frequency of Spontaneous Swallowing. *Conf Proc Australas Phys Eng Sci Med* 2007;30(4):313-317.
30. Smith S, Jenkinson M, Woolrich M, Beckmann C. Advances in functional and structural MR image analysis and implementation as FSL. *Neuroimage* 2004;23:S208-S219.
31. Jenkinson M, Bannister P, Brady M, Smith S. Improved optimization for the robust and accurate linear registration and motion correction of brain images. *Neuroimage* 2002;17:825-841.
32. Smith SM. Fast robust automated brain extraction. *Hum Brain Mapp* 2002;17(3):143-155.
33. Worsley KJ. Statistical analysis of activation images. In: P. Jezzard PMM, S. M. Smith, editor. *Functional MRI: An Introduction to Methods*: Oxford University Press; 2001.
34. Lancaster JL, Tordesillas-Gutiérrez D, Martinez M, Salinas F, Evans A, Zilles K, Mazziotta JC, Fox PT. Bias between MNI and Talairach coordinates analyzed

- using the ICBM-152 brain template. *Hum Brain Mapp* 2007;28(11):1194-1205.
35. Toogood J, Barr A, Stevens T, Gati J, Menon R, Martin R. Discrete functional contributions of cerebral cortical foci in voluntary swallowing: a functional magnetic resonance imaging (fMRI) "Go, No-Go" study. *Exp Brain Res* 2005;161:81-90.
 36. Shinagawa H, Ono T, Honda E-I, Masaki S, Shimada Y, Fujimoto I, Sasaki T, Iriki A, Ohyama K. Dynamic analysis of articulatory movement using magnetic resonance imaging movies: methods and implications in cleft lip and palate. *Cleft Palate Craniofac J* 2005;42(3):225-230.
 37. Birn R, Bandettini PA, Cox R, Jesmanowicz A, Shaker R. Magnetic field changes in the human brain due to swallowing or speaking. *Magn Reson Med* 1998;40:55-60.
 38. Gracco V, Tremblay P, Pike B. Imaging speech production using fMRI. *Neuroimage* 2005;26(1):294-301.
 39. Malandraki G, Sutton B, Perlman A, Karampinos D. Age-related differences in laterality of cortical activations in swallowing. *Dysphagia* 2009;1-12.
 40. Eden G, Joseph J, Brown H, Brown C, Zeffiro T. Utilizing hemodynamic delay and dispersion to detect fMRI signal change without auditory interference: the behavior interleaved gradients technique. *Magn Reson Med* 1999;41(1):13-20.
 41. Sutton BP, Noll DC, Fessler JA. Dynamic field map estimation using a spiral-in/spiral-out acquisition. *Magn Reson Med* 2004;51(6):1194-1204.
 42. Sekihara K, Kuroda M, Kohno H. Image restoration from non-uniform magnetic field influence for direct Fourier NMR imaging. *Phys Med Biol.* 1984;29(1):15-24.
 43. Jezzard P, Balaban RS. Correction for geometric distortion in echo planar images from B0 field variations. *Magn Reson Med.* 1995;34:65-73.
 44. Schomberg H. Off-resonance correction of MR images. *IEEE Trans Med Imaging.* 1999;18(6):481-95.
 45. Frahm J, Merboldt KD, Hanicke W. Direct FLASH MR imaging of magnetic field inhomogeneities by gradient compensation. *Magn Reson Med.* 1988;6(4):474-80.
 46. Constable RT. Functional MR imaging using gradient-echo echo-planar imaging in the presence of large static field inhomogeneities. *J Magn Reson Imaging.* 1995;5(6):746-52.
 47. Glover GH. 3D z-shim method for reduction of susceptibility effects in BOLD fMRI. *Magn Reson Med.* 1999;42(2):290-9.
 48. Reichenbach JR, Venkatesan R, Yablonskiy DA, Thompson MR, Lai S, Haacke EM. Theory and application of static field inhomogeneity effects in gradient-echo imaging. *J Magn Reson Imaging.* 1997;7(2):266-79.
 49. Maeda A, Sano K, Yokoyama T. Reconstruction by weighted correlation for MRI with time-varying gradients. *IEEE Trans Med Imaging.* 1988;7(1):26-31.

50. Noll DC, Fessler JA, Sutton BP. Conjugate phase MRI reconstruction with spatially variant sample density correction. *IEEE Trans Med Imaging*. 2005;24(3):325-36.
51. Deichmann R, Josephs O, Hutton C, Corfield DR, Turner R. Compensation of susceptibility-induced BOLD sensitivity losses in echo-planar fMRI imaging. *NeuroImage*. 2002;15(1):120-35.
52. Krishnan S, Noll DC. Effects of local susceptibility gradients on spiral k-space trajectory and effective echo-time (TE_{eff}). *Proc 14th Intl Soc Magn Reson Med Seattle, WA 2006*. p. 2823.
53. Li TQ, Takahashi A, Wang Y, Mathews V, Glover GH. Dual-echo spiral in/in acquisition method for reducing magnetic susceptibility artifacts in blood-oxygen-level-dependent functional magnetic resonance imaging. *Magn Reson Med*. 2006;55(2):325-34.
54. Fera F, Yongbi MN, van Gelderen P, Frank JA, Mattay VS, Duyn JH. EPI-BOLD fMRI of human motor cortex at 1.5 T and 3.0 T: sensitivity dependence on echo time and acquisition bandwidth. *Journal of magnetic resonance imaging : JMRI*. 2004;19(1):19-26.
55. Chang C, Thomason ME, Glover GH. Mapping and correction of vascular hemodynamic latency in the BOLD signal. *NeuroImage*. 2008;43(1):90-102. PMID: PMC2587338.
56. Thomason ME, Foland LC, Glover GH. Calibration of BOLD fMRI using breath holding reduces group variance during a cognitive task. *Human brain mapping*. 2007;28(1):59-68.
57. Goh JO, Suzuki A, Park DC. Reduced neural selectivity increases fMRI adaptation with age during face discrimination. *NeuroImage*. 2010;51(1):336-44. PMID: 2847054.
58. Jenkinson M, Smith S. A global optimisation method for robust affine registration of brain images. *Medical image analysis*. 2001;5(2):143-56.
59. Jenkinson M, Bannister P, Brady M, Smith S. Improved optimization for the robust and accurate linear registration and motion correction of brain images. *NeuroImage*. 2002;17(2):825-41.
60. Woolrich MW, Ripley BD, Brady M, Smith SM. Temporal autocorrelation in univariate linear modeling of FMRI data. *NeuroImage*. 2001;14(6):1370-86.
61. Collins DL, Holmes CJ, Peters TM. Automatic 3-D model-based neuroanatomical segmentation. *Human brain mapping*. 1995;3(3):190-208.
62. Mazziotta J, Toga A, Evans A, Fox P, Lancaster J, Zilles K, Woods R, Paus T, Simpson G, Pike B, Holmes C, Collins L, Thompson P, MacDonald D, Iacoboni M, Schormann T, Amunts K, Palomero-Gallagher N, Geyer S, Parsons L, Narr K, Kabani N, Le Goualher G, Boomsma D, Cannon T, Kawashima R, Mazoyer B. A probabilistic atlas and reference system for the human brain: International consortium for brain mapping (ICBM). *Phil Trans R Soc Lond B*. 2001;356:1293-322.
63. Pipe JG. Spatial encoding and reconstruction in MRI with quadratic phase profiles. *Magn Reson Med*. 1995;33(1):24-33.
64. Wedeen VJ, Chao YS, Ackerman JL. Dynamic range compression in MRI by means of a nonlinear gradient pulse. *Magn Reson Med*. 1988;6(3):287-95.

65. Ito S, Yamada Y. Alias-free image reconstruction using Fresnel transform in the phase-scrambling Fourier imaging technique. *Magn Reson Med.* 2008;60(2):422-30.